



**Thermal Transport through Fishbone Silicon Nanoribbons:
Unraveling the Role of Sharvin Resistance**

Journal:	<i>Nanoscale</i>
Manuscript ID	NR-ART-03-2019-001855.R1
Article Type:	Paper
Date Submitted by the Author:	02-Apr-2019
Complete List of Authors:	Yang, Lin; Vanderbilt University, Mechanical Engineering Zhao, Yang; Vanderbilt University, Mechanical Engineering Zhang, Qian; Hermes-Microvision Inc., ; Vanderbilt University College of Arts and Science, Mechanical Engineering Yang, Juekuan; Southeast University, Mechanical Engineering Li, Deyu; Vanderbilt University, Mechanical Engineering

Thermal Transport through Fishbone Silicon Nanoribbons: Unraveling the Role of Sharvin Resistance

Lin Yang,¹ Yang Zhao,¹ Qian Zhang,¹ Juekuan Yang,² and Deyu Li^{1,}*

¹Department of Mechanical Engineering, Vanderbilt University, Nashville, TN 37235, USA

²School of Mechanical Engineering and Jiangsu Key Laboratory for Design and Manufacture of Micro-Nano Biomedical Instruments, Southeast University, Nanjing, 211189, P. R. China

*Author to whom correspondence should be addressed. E-mail: deyu.li@vanderbilt.edu

Abstract: Heat conduction has been shown to be greatly suppressed in Si nanomeshes, which has attracted extensive attention for potential thermoelectric applications, yet the precise suppression mechanism remains to be fully understood. Attempting to further disclose the underlying mechanisms, we report on the thermal conductivity of the building block for nanomeshes, i.e., Si nanoribbons with fins attached to the two opposite sides. By expanding only the fin width while keeping both the period length and backbone size constant, we observed an unexpected non-monotonic trend of the effective thermal conductivity normalized with the backbone cross-section. Further analysis showed that the corrected thermal conductivity extracted with proper consideration of the geometrical effect on diffusion followed a monotonically decreasing trend, reaching a maximum thermal conductivity reduction of 18% at 300 K for a ribbon with the maximum explored fin width of 430 nm, as compared to that of the straight ribbon of 66 nm backbone width. We attribute the thermal conductivity reduction to the thermal constriction resistance induced by the cross-section reduction between the fin and backbone sections. For ribbons with larger fin width, the effective phonon mean free path is longer for phonons arriving at the constriction, which boosts the ballistic constriction resistance, i.e., Sharvin resistance, and leads to a lower thermal conductivity.

Keywords: Si fishbone nanoribbons, Si nanomesh, thermal conductivity, nanoscale constriction, Sharvin resistance

Introduction

Understanding thermal transport through various nanostructures of silicon, the most widely used semiconductor material, has attracted a great deal of attention in the past two decades as it is critical for many applications.¹⁻⁵ For example, recognizing the opportunity of massive production through either bottom-up synthesis or top-down microfabrication approaches, significant efforts have been devoted to prepare silicon nanostructures with drastically reduced thermal conductivity as high-performance, scalable thermoelectric materials.⁴⁻⁷ Although bulk Si is a poor thermoelectric material due to its rather high thermal conductivity, a remarkable improvement has been achieved with rough Si nanowires, demonstrating a figure-of-merit (ZT) of ~ 0.6 , nearly two orders of magnitude higher than that for bulk Si.⁴ For most studies, including those on Si thin films^{8,9} and nanowires^{10,11} or rough nanowires,^{4,12} the thermal conductivity reduction has been attributed to scattering of phonons at thermal boundaries that leads to enhanced phonon scattering rates, following the phonon particle picture. On the other hand, through fabricating thin Si meshes with periodic nanoscopic holes, it has been suggested that taking advantage of the phonon wave nature can further suppress thermal transport by reshaping the phonon band structures.¹³⁻¹⁶ For instance, a room-temperature thermal conductivity of 1.9 W/m-K has been achieved for a 22 nm thick Si nanomesh, approaching the amorphous limit of ~ 1 W/m-K.¹³

Although the prospect of exploiting the phonon wave properties could hold promise for potential phononic applications, recent theoretical and experimental results cast doubts on the importance of phonon coherence in Si nanomeshes.¹⁷⁻¹⁹ For example, Jain et al. calculated the thermal conductivities of Si nanomeshes using a Monte Carlo method, and by considering only the phonon boundary scattering effect, their results captured the magnitudes and trends of the experimental data quite well.¹⁷ More recently, Lee et al. tried to isolate the contribution of wave

effects by comparing the measured thermal conductivity of Si meshes with periodic and aperiodic hole arrangements; however, the identical thermal conductivity values for these two cases suggest that above 14 K phonon coherence does not play any significant role in Si nanomeshes with period lengths larger than 100 nm.¹⁹ Instead, phonon backscattering, a picture based on phonon particle transport, is believed to be responsible for the thermal conductivity reduction.^{19–21}

In explaining thermal transport through nanomeshes, it has been claimed that ballistic phonons travelling to the neck areas are likely to be scattered backwards. As such, the thermal conductivity reduction is attributed to the trapped phonon modes induced by the backscattering effect.^{19–21} Alternatively, we believe that the underlying physics can be understood from another perspective and quantitatively described by employing the concept of ballistic constriction resistance, i.e., Sharvin resistance.^{22,23} For Si nanomeshes with periodic holes, each neck area can be regarded as a geometrical constriction, and when the phonon mean free path (mfp) is longer than the neck width, Sharvin resistance would pose additional impedance to phonon transport.^{23,24}

To unravel the role of Sharvin resistance, we investigate thermal transport through the building block of Si nanomeshes with aligned holes,⁵ i.e., straight Si nanoribbons with fins attached to the two opposite sides, which form the fishbone structure that has been studied by Nomura *et al.* in several reports.^{25–27} Different from previous experimental studies on Si nanomeshes,^{13,14,19–21} we keep both the period length and backbone size the same and only vary the fin width. The corrected thermal conductivity, extracted with proper consideration of the geometrical effect on diffusive phonon transport, demonstrates a monotonically decreasing trend as the fin width increases, reaching a maximum thermal conductivity reduction of 18% at 300 K for a ribbon with the largest explored fin width of 430 nm, as compared to that of a straight ribbon of 66 nm backbone width. As both the period length and limiting dimension are kept the same,

the reduced thermal conductivity should not be the result of either phonon coherence or stronger phonon boundary scattering. Instead, expanding the fin width effectively elongates the mfp of phonons before they arrive at the constriction area, which leads to enhanced ballistic constriction resistance, and hence lower thermal conductivities for fishbone Si nanoribbons with wider fin width.

Results and discussion

In the experiment, we fabricated single crystalline Si fishbone nanoribbons using electron-beam lithography (EBL) from a silicon-on-insulator (SOI) wafer.^{11,28} To pattern nanostructures with tightly arranged features of widely varying sizes, such as fishbone nanoribbons, proximity effect correction was performed to ensure the target electron energy distribution of the design matches as precisely as possible the actual energy requirement.²⁹ As shown in the SEM images in Fig. 1a, five different Si fishbone nanoribbons were fabricated to have the same backbone width (w_b , typically 68 ± 2 nm s.d. between samples), but different fin width (w_f , from 121 to 430 nm). Other dimensions, including the period ($p = 307 \pm 4$ nm), fin length ($l_f = 149 \pm 5$ nm), as well as the backbone length in each period ($l_b = 159 \pm 4$ nm), are kept approximately the same. Fig. 1b shows a 3D profile of the nanoribbon sample ($w_f = 312$ nm) obtained via atomic force microscopy (AFM, Bruker Dimension Icon), from which the thickness is measured as 38 nm. Owing to the existence of ~ 2 nm-thick native oxide layers on both the top and bottom surfaces, the thickness of the Si core layer, t , is taken as 34 nm. To quantitatively evaluate the fin effects on phonon transport, a straight Si nanoribbon with a width of 66 nm was also fabricated to serve as a baseline sample. The detailed geometries of all samples are summarized in Table 1. After the as-fabricated nanoribbons were transferred to a piece of polydimethylsiloxane (PDMS) through a stamping

transfer process,^{11,30} an in-house built micromanipulator was used to pick up the sample with a sharp probe and placed it between two suspended micro-membranes in the measurement device for subsequent thermal measurements,^{10,31–34} as shown in Fig. 1c. Note that owing to the flat contact between the nanoribbon and Pt electrodes, the relatively large contact area as compared to the nanoribbon cross-section leads to a negligible contact thermal resistance.^{11,35}

Fig. 2a plots the measured room-temperature thermal conductivity of the Si fishbone nanoribbons in comparison to that of the baseline straight ribbon (shown as the dash dotted line). Here the blank squares represent the effective thermal conductivity, κ_{eff} , extracted based on the cross-section dimension of the backbone width and ribbon thickness. It can be seen that κ_{eff} is higher than that of the straight ribbon, which is different from the reported results of a SiC nanowire with periodically modulated cross-section studied using molecular dynamics (MD).³⁶ In that case, the effective thermal conductivity of the modulated SiC nanowires derived based on the smaller section's area was lower than that of the corresponding wire with an equal and uniform cross-section, which was attributed to the additional resistance at the constrictions.³⁶

Interestingly, the effective thermal conductivity of the Si nanoribbons shows a non-monotonic trend as the fin width increases, with κ_{eff} increasing with the fin width before w_f reaches 216 nm, and then decreasing as w_f further extends. This non-monotonic variation is out of our expectation because one would normally anticipate that as the fin gets wider, the additional volume contributes less to thermal transport and κ_{eff} approaches asymptotically to a maximum value, similar to the case as discussed with respect to the thermally dead volume in Si nanoladders.³⁷ However, the decreasing trend as w_f becomes larger than 216 nm cannot be explained by the concept of thermally dead volume as it will not further affect the thermal conductance and hence the effective thermal conductivity.

The effective thermal conductivity is always higher than the corresponding value of the straight ribbon of backbone width; therefore, it is clear that the larger cross-sectional area at the fin section facilitates heat flow. As such, without taking into account of the cross-sectional size variation, i.e., using the backbone cross-sectional area to extract thermal conductivity, results in higher effective thermal conductivity. However, the non-monotonic dependence of κ_{eff} on the fin width indicates that effects beyond pure diffusion has to play a role. To disclose this non-diffusion mechanism, we have to properly account for the size variation in interpreting the measured data. The effects of size variation on pure diffusion transport should be the same for nanoribbons or bulk ribbons as long as the entire structure scale proportionally. As such, we introduce a correction factor to the cross-sectional area, f , through finite element method (FEM) simulations using the ANSYS® software on bulk beams that are scaled by 10^6 in size. For the bulk beams, we can safely take their thermal conductivities as the bulk value and based on the obtained heat flux as well as the imposed temperature difference, the thermal conductance can be easily derived. The correction factor, f , can then be readily defined as the ratio of the thermal conductance of the beams with different fin geometries to that of the corresponding straight beam without fins.

We note that other approaches of defining the correction factor could be introduced. For example, one potential way is based on equivalent volume, with an effective width defined as $w_{eff} = (w_b \times l_b + w_f \times l_f)/(l_b + l_f)$ and the correction factor defined as $f = w_{eff}/w_b$. This approach gives a much larger correction factor than what we obtained from the FEM modeling because the outer edges of the fin section contribute less to the heat conduction, so giving the same weight to all the volume in considering the contribution of the fin section severely over-estimates the correction factor. Another approach was adopted by Nomura *et al.*²⁶ in their studies of thermal transport through fishbone nanoribbons, which is based on equivalent thermal resistance. In their

calculation, the thermal conductivity is derived based on an effective width that is defined as $w_{eff} = \left(\frac{l_b}{w_b} + \frac{l_f}{w_f}\right)^{-1} (l_b + l_f)$,³⁸ and the correction factor can also be regarded as $f = w_{eff}/w_b$. We note that the above treatment assumes that the fin and backbone sections as well as the unit cell in the fishbone structure possess the same thermal conductivity, which neglects the difference of the effective phonon mfp in the fin and backbone sections. As such, our approach of defining the cross-section, i.e., introducing a correction factor to consider the effects of geometrical variation purely based on diffusive transport, better distinguishes the impacts of factors other than diffusion. The calculated correction factor is also plotted in Fig. 2a, which increases as the fin width expands (See Supplementary Information for comparison of correction factors from different approaches). The corrected thermal conductivity, κ_{corr} , can then be calculated as $\kappa_{corr} = GL/(fw_b t)$, where G and L are the measured thermal conductance and the length of the sample between the two suspended membranes, respectively.

The room-temperature κ_{corr} is also plotted in Fig. 2a as the filled squares, which exhibits a continuously decreasing trend as the fin width increases and is lower than that of the straight ribbons for all cases. A thermal conductivity reduction ratio, $(\kappa_{straight} - \kappa_{fishbone})/\kappa_{straight}$, can be defined, which enlarges from 2% to 18% at 300 K as w_f expands from 121 to 430 nm. Note that even for the sample with the widest fins ($w_f = 430$ nm), radiation from the sample to the surrounding is still three orders of magnitude lower than heat conduction through the sample at 300 K; thus, it is indeed the nanoscale geometric effect causing the lower corrected thermal conductivity in the Si fishbone nanoribbons. To show the thermal transport behavior in a wider temperature range, we plot κ_{corr} from 50-350 K in Fig. 2b. The calculated thermal conductivity reduction ratio increases as temperature reduces, and for $w_f = 430$ nm, it rises to 26% at 50 K. We note that the calculated surface-area-to-volume ratio (S/V) of the fishbone nanoribbons are all

lower than that of the straight ribbon, and in fact, it reduces as the fin width expands (Table 1). As nanostructures with lower S/V experience weaker phonon boundary scattering effect,¹¹ an increase trend in thermal conductivity would be expected for wider fins if we only consider the classical size effect, which is, however, opposite to our experimental observation.

To further understand phonon transport in fishbone nanoribbons, we consider the thermal resistance of a unit cell, as shown in Fig. 2c. The thermal resistance network of the unit cell includes those of the backbone R_b , the fin section R_f , and the constriction R_c , which connect in series, as shown at the bottom of Fig. 2c. Thus, we can calculate R_c according to

$$R_c = \frac{1}{2} \left(\frac{1}{G_u} - \frac{l_b}{k_b A_b} - \frac{l_f}{k_f A_f} \right), \quad (1)$$

where G_u is the measured thermal conductance of a unit cell, $l_{b/f}$, $A_{b/f}$, $k_{b/f}$ are the length, cross-sectional area, and thermal conductivity of backbone/fin section, respectively. The room-temperature thermal conductivity of the fin section is obtained based on the calculated S/V ratio of the fin section.¹¹

Fig. 2d plots the extracted room-temperature thermal resistance of the constriction, backbone and fin, respectively. It can be seen that the primary thermal resistance stems from the narrow backbone due to the strong phonon boundary scattering, and it only changes marginally across different samples, which is due to the slight backbone width difference caused by inevitable variations during nanofabrication. In addition, as the fin width expands, thermal resistance of the fin section decreases, but the constriction resistance induced by the cross-section change increases significantly. Therefore, as shown in Fig. 2a, the calculated κ_{eff} first increases with the fin width due to the reduced total thermal resistance caused by the lower fin section resistance. However, for w_f wider than 216 nm, the enhancement of R_c more than compensates the reduction of R_f and

therefore, the total thermal resistance starts to escalate, which explains the observed peak effective thermal conductivity.

It is usually illustrative to compare the constriction resistance with the Kapitza resistance at the interface between two different solids.^{39–41} The extracted constriction resistance for unit cross-sectional area ranges from $0.52\text{--}1.81 \times 10^{-9}$ m²-K/W for the five different Si fishbone nanoribbons at 300 K, which converts to an interfacial thermal conductance (ITC) of 552–1923 MW/m²-K. This level of resistance is not trivial, as for the interface between TiN/MgO (both with similar Debye temperature, θ_D), the measured ITC is ~ 700 MW/m²-K at 300 K;³⁹ and for the Au/Si multilayer nanostructures ($\theta_{Au} = 165$ K, $\theta_{Si} = 640$ K), which represents a highly mismatched system in inorganic multilayers, the room-temperature ITC is shown to be ~ 100 MW/m²-K.⁴⁰ Therefore, our extracted constriction resistance is on the same order as common interfacial thermal resistance between inorganic materials.

The constriction resistance at nanoscale contacts between two solid materials has been investigated previously;^{23,42–44} and when the phonon mfp is comparable to the characteristic size of the constriction area, the total thermal constriction resistance, including both diffusive and ballistic components, is approximated as:^{22,23}

$$R_c = R_{cd} + R_{cb} = \frac{1}{2\kappa a} + \frac{4\Lambda}{3\kappa A_c}. \quad (2)$$

Here, κ is the thermal conductivity of the semi-infinite objects; a is the radius of the contact; A_c is the constriction area; and Λ is phonon mfp. R_{cd} denotes the diffusive constriction resistance, caused by the heat flux lines' constriction in the vicinity of the constriction, while R_{cb} (ballistic constriction resistance, i.e., Sharvin resistance) is the resistance when phonon mfp is much larger than the contact radius, a . For our Si fishbone nanoribbons, the nanoscale constriction forms owing to the cross-section dimension reduction between the fin and backbone sections. Although R_{cd} remains

nearly constant due to the constant backbone width, as the fin width w_f expands, phonons would have longer mfp in the fin section and as a result, R_{cb} increases with w_f , which is consistent with the results in Fig. 2d. It is important to note that even though the smallest dimension of the nanoribbon is its thickness (34 nm), confinement from the two side walls still significantly affect the phonon mfp, as demonstrated in our recent study of thermal transport through different aspect ratio nanoribbons.¹¹ In fact, the confinement effect from the two side walls is clearly illustrated by the ratio of the reduction function of nanoribbons to that of a thin film of the same thickness, as shown in the Supplementary Information. Moreover, phonon mfp increases at lower temperatures, which leads to enhanced R_{cb} and more significant thermal conductivity reduction observed for each Si fishbone samples, as depicted in Fig. 2b.

We note that the constriction in the fishbone Si nanoribbons only confines the cross-sections along the width direction, not like the diameter modulated nanowires that have been investigated by theoretical modeling.^{36,45,46} As mentioned previously, Termentzidis et al. modeled thermal transport in diameter modulated SiC nanowires using MD,³⁶ which showed effective thermal conductivities lower than that of the corresponding small cross-section nanowire. We believe that this could be explained by the stronger constriction effect in the diameter modulated SiC nanowires. For the Si fishbone nanoribbon with $w_f = 430$ nm, the constriction resistance counts for 31% of the total thermal resistance, while the thermal constriction resistance represents 65% of the total resistance in the SiC nanowire with a cross-section combination of 15.67-35.25 nm².³⁶

To further understand thermal transport in Si fishbone nanoribbons with geometric constriction only in the width direction, we also performed non-equilibrium MD (NEMD) simulations. The NEMD simulations were carried out using the well-established LAMMPS package; and the Stillinger-Weber (SW) potential was adopted to describe the interaction between

silicon atoms.⁴⁷ The Newton equations of motion for each atom were numerically solved using the velocity Verlet algorithm with an integration time step of 0.5 fs and the total simulation time is 20 ns. In the simulation, fixed boundary conditions are applied in the axial direction, and free boundary conditions are applied in the lateral directions. The two regions close to the left/right ends are designed as the hot and cold reservoirs with temperatures controlled by the Langevin thermostat.⁴⁸ Note that the geometry of the modeled fishbone nanoribbons mimics the as-fabricated samples, but the size is scaled to be ~20 times smaller due to the limitation on system size in NEMD simulations. To best resemble the experimental case, we only vary the fin width (from 6.5 to 13 nm) while keeping all other parameters the same (backbone width is kept as 3.3 nm).

Fig. 3a plots the modeled temperature distribution along the axial direction of the Si fishbone nanoribbon. Instead of following a continuous temperature gradient, two abrupt temperature drops between the backbone and fin section could be clearly discerned. More importantly, as the fin width increases, the magnitude of the temperature drop, and hence the constriction thermal resistance, increases. From the modeled temperature distribution and the calculated heat transfer rate, we can extract the thermal resistance for each section. At 300 K, as the fin width increases from 6.5 to 13 nm, the thermal resistance of the backbone R_b remains nearly the same, and R_f reduces from 6.47×10^7 to 3.05×10^7 K/W; however, R_c increases from 1.89×10^7 to 3.64×10^7 K/W.

To examine the detailed lattice vibration characteristics across the constriction, similar to the approach used by Termentzidis et al.,³⁶ we selected four slabs of atoms as indicated in Fig. 3b and calculated the phonon DOS in the frequency range of 0~20 THz. The resulting phonon DOS for position 1 and 4 (P1&4) essentially overlaps with each other due to the same limiting dimension (thickness). However, we do observe distinct vibrational properties for silicon atoms at P2 and

P3. First, the peak intensities for the transverse optical (TO) branch at P2 and P3 are different from that at P1&4, which could be explained by the altered surface stress, as demonstrated in Ge nanoparticles.⁴⁹ At the first layer in the fin section (P3), the atoms are weakly bonded surface atoms, and the slight lattice expansion would result in softening of interatomic force constant, which leads to the reduced TO peak intensity.⁴⁹ In contrast, for Si atoms at P2, especially those at the corners, they could interact with the nearby atoms at the fin surface, and exhibit an enhanced TO peak intensity.⁴⁹ More importantly, for atoms at the first layer in the fin section (P3), the transverse acoustic (TA) peak shifts to lower frequencies. This could be explained as the mfp of low frequency phonons is much larger than the constriction size, only phonons pointing to the small constriction area could directly pass through (Fig. 2c), and the blocked phonons form stationary modes, leading to the peak shifting to lower frequencies. In fact, the existence of the confined phonon modes has also been observed in the width modulated SiC nanowires.³⁶ As shown in Fig. 3d, when w_f increases from 6.5 to 13 nm, a greater mismatch between the phonon DOS distributions at P2 and P3 could be observed, which helps to account for the observed increasing thermal constriction resistance.

As mentioned previously, Si fishbone nanoribbon could be regarded as the building block for Si nanomeshes with aligned hole arrangement (inset in Fig. 1a), and investigating thermal conductivity reduction mechanisms in fishbone nanoribbons could help to further understand the low thermal conductivities of nanomeshes. In general, previous reports have suggested three different strategies to suppress thermal transport in Si nanomeshes, namely (i) decreasing both the neck width and period length (neck is the backbone part in the fishbone nanoribbons);^{13,14,20} (ii) decreasing neck width while keeping period length constant;²¹ (iii) keeping neck width constant while reducing the period length.¹⁹ For nanomeshes with reducing neck width (i&ii), the

constriction area becomes smaller, and according to Eq. (2), both diffusive and ballistic constriction resistance would increase. On the other hand, nanomeshes with shorter period length (i&iii) would increase the constriction scattering center density. Therefore, all these strategies are consistent with enhancing the thermal constriction resistance of the neck.

Conclusions

In summary, we investigate thermal transport through the building block of Si nanomeshes, i.e., straight Si nanoribbons with fins attached to the sides, to understand the underlying mechanisms of the reduced thermal conductivity observed for Si nanomeshes. The results show an unexpectedly low thermal conductivity, which after properly taking into account the geometrical size variation, becomes a monotonically reduced thermal conductivity for wider fin width samples while keeping all of the rest dimensions the same. We attribute this to the ballistic constriction resistance induced by the cross-section dimension reduction between the fin and backbone sections, as manifested by the temperature distribution discontinuity near the constriction area in MD simulations. This work provides additional insights for the design of complicated nanostructured geometries for thermoelectric applications.

Table 1. Summary of the geometry of Si fishbone nanoribbons and the obtained corrected thermal conductivity at 300 K.^a

	backbone length, l_b (nm)	backbone width, w_b (nm)	fin length, l_f (nm)	fin width, w_f (nm)	S/V (nm ⁻¹)	κ_{corr} (W/m-K)
#1	164	68	140	121	0.084	21.1 (± 1.96)
#2	157	66	155	158	0.082	20.4 (± 1.75)
#3	162	68	148	216	0.080	19.6 (± 1.87)
#4	152	67	148	312	0.078	18.8 (± 1.72)
#5	158	72	152	430	0.076	17.7 (± 1.56)
straight		66			0.089	21.6 (± 1.99)

^aAll samples are 34 nm in Si core thickness. All κ_{corr} are corrected values using the correction factor f .

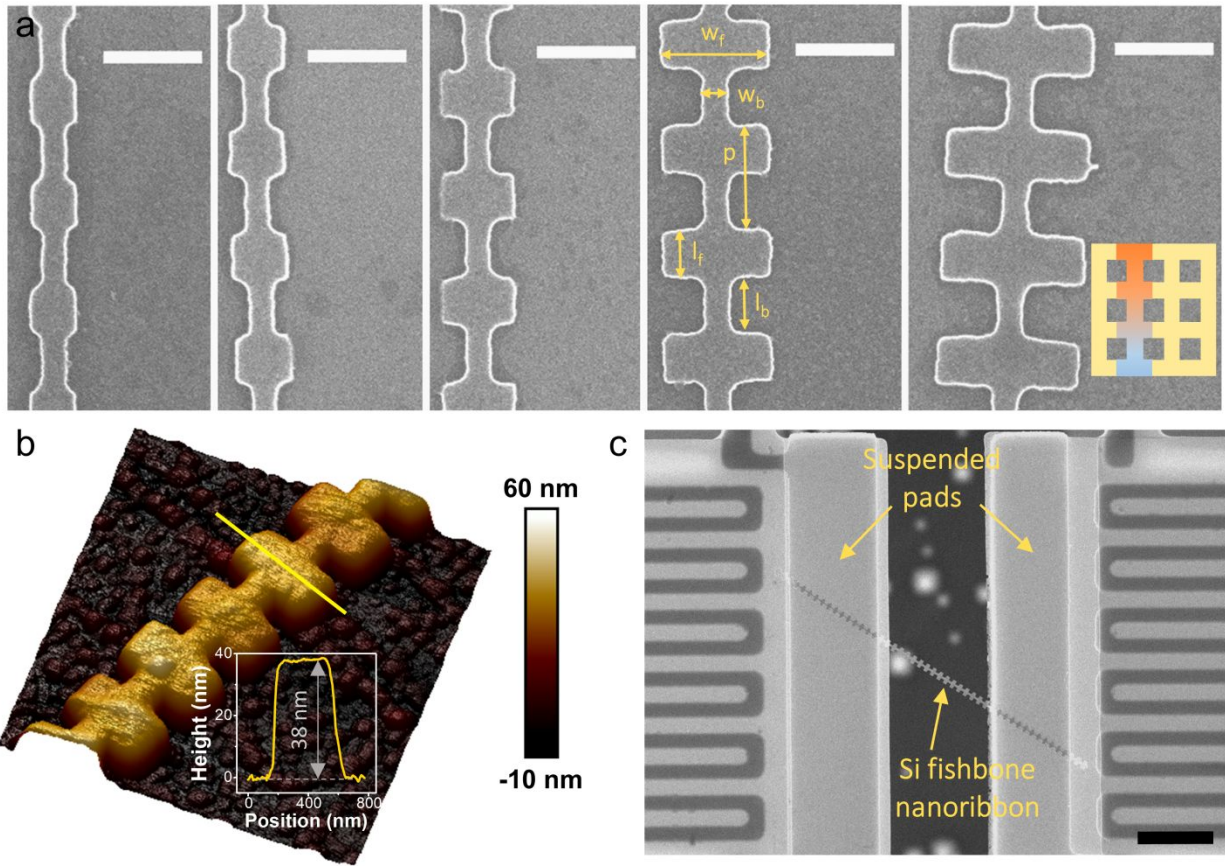


Figure 1. (a) SEM micrographs showing the as-fabricated Si fishbone nanoribbons, where all dimensions are kept the same but only the fin width, w_f , is changed across different samples. The inset image shows that fishbone nanoribbons could be regarded as building blocks for nanomeshes with aligned hole arrangement. (b) A 3D AFM scanning result showing the profile of the fabricated Si fishbone nanoribbons ($w_f = 312$ nm). (c) An SEM image showing a fishbone nanoribbon sample ($w_f = 312$ nm) after transferred to bridge the two membranes of the suspended microdevice. Scale bars: 300 nm in (a) and 3 μ m in (c).

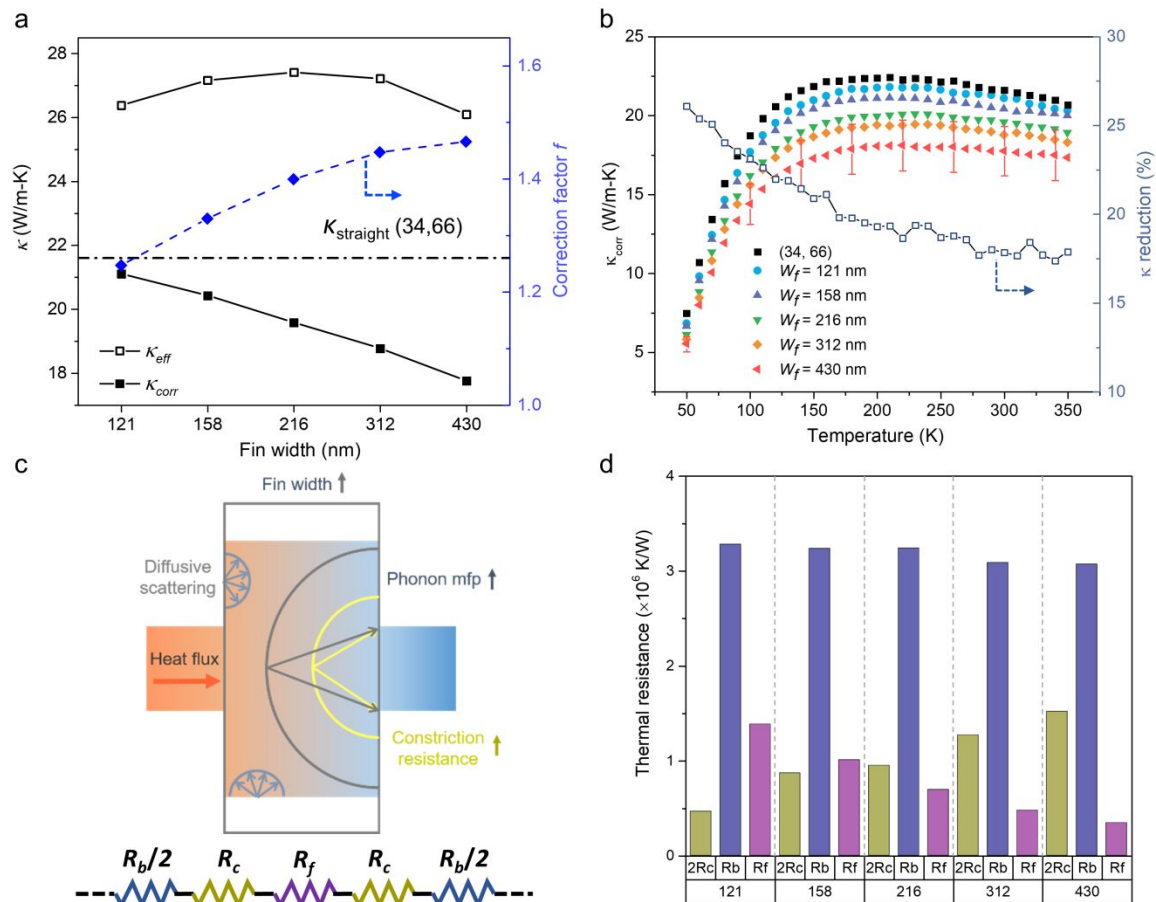


Figure 2. (a) Measured room-temperature effective thermal conductivity κ_{eff} of the Si fishbone nanoribbons with the cross-sections as the backbone width and ribbon thickness, where κ_{eff} is calculated based on the cross-section dimension of the backbone width and ribbon thickness. The corrected thermal conductivity value κ_{corr} is calculated after κ_{eff} is normalized with the correction factor f (right axis). The measured room-temperature thermal conductivity of the straight ribbon (34 nm thickness and 66 nm width) is also plotted for comparison as the dash dotted line. (b) Temperature dependent corrected thermal conductivity for five different Si fishbone nanoribbons, where the measured κ of the straight ribbon is also plotted for comparison. The calculated thermal conductivity reduction for the fishbone nanoribbon with the fin width of 430 nm is plotted as a function of temperature (right axis). (c) Schematic diagram showing the ballistic thermal constriction resistance. Within the hemisphere of the ballistic phonon mean free path, only phonons pointing to the small constriction can pass through. The bottom panel is an illustration of the thermal resistive network. (d) Extracted thermal resistance of the constriction (R_c), backbone (R_b) and fin section (R_f) for five Si fishbone nanoribbons at 300 K.

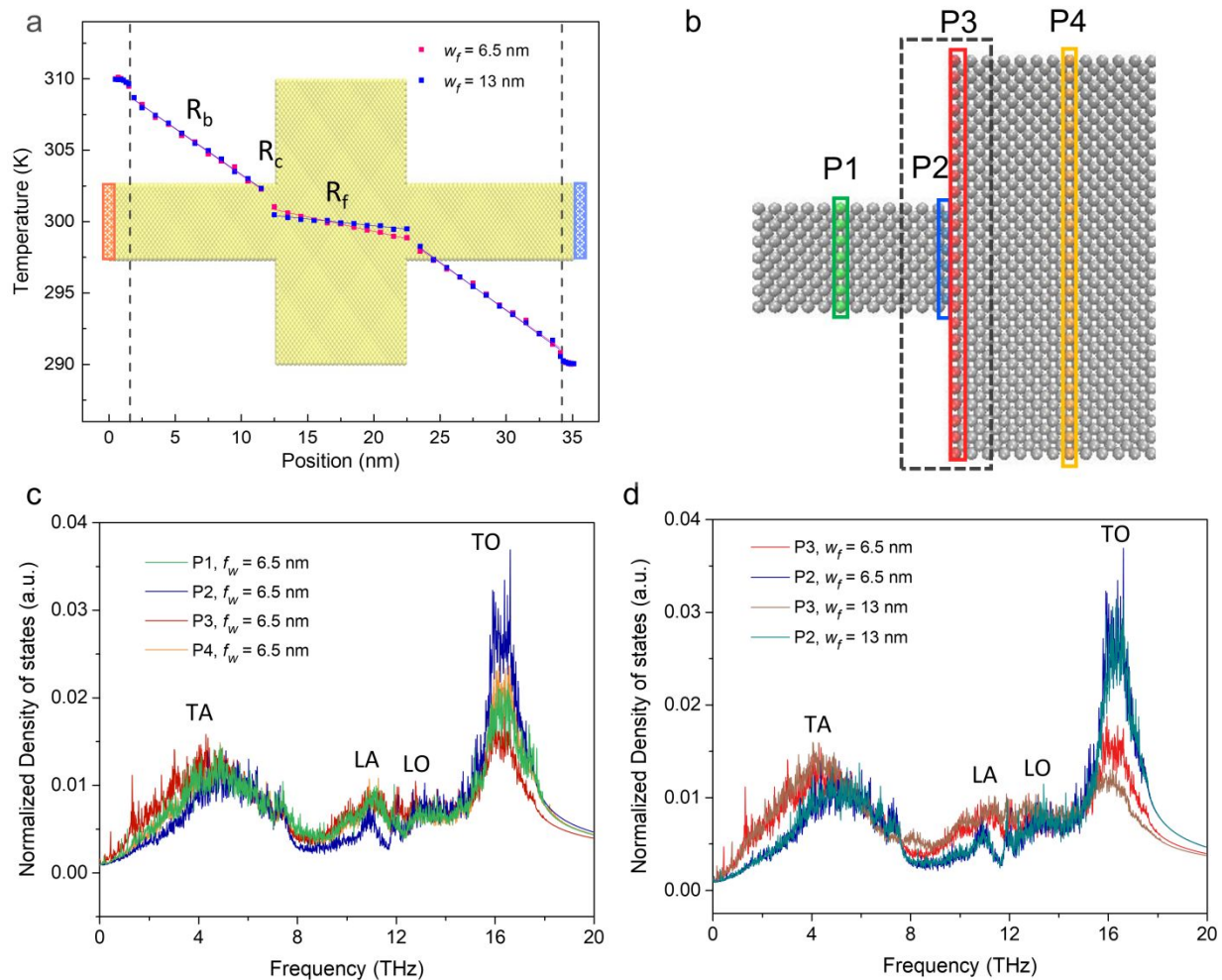


Figure 3. Molecular dynamics simulation results. (a) Simulated temperature distribution along the axial direction of the fishbone nanoribbons with fin width of 6.5 and 13 nm. (b) The four considered groups for the calculation of the phonon density of states, highlighted as P1, P2, P3, and P4 from left to right. (c) Comparison of the calculated phonon density of states at positions P1-4 for fin width of 6.5 nm. (d) Comparison of the phonon DOS at P2 and P3 when the fin width is increased from 6.5 to 13 nm.

Conflicts of interest

There are no conflicts of interest to declare.

Acknowledgements

The authors acknowledge the financial support from the U.S. National Science foundation (CBET-1403456; DMR-1532107; and CBET-1805924). J.Y. acknowledges the financial support from National Key R&D Program of China (Grant# 2017YFB0406000).

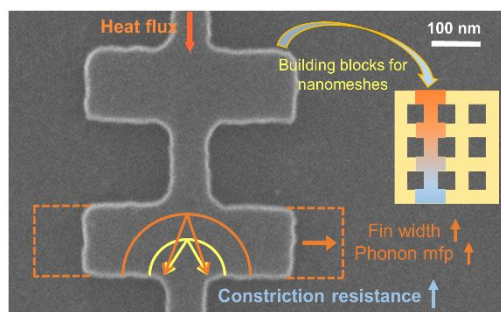
Notes and references

- 1 Y.-F. Huang, S. Chattopadhyay, Y.-J. Jen, C.-Y. Peng, T.-A. Liu, Y.-K. Hsu, C.-L. Pan, H.-C. Lo, C.-H. Hsu, Y.-H. Chang, C.-S. Lee, K.-H. Chen and L.-C. Chen, *Nanotechnol.*, 2007, **2**, 770–774.
- 2 M. T. Björk, H. Schmid, J. Knoch, H. Riel and W. Riess, *Nat. Nanotechnol.*, 2009, **4**, 103–107.
- 3 F. Priolo, T. Gregorkiewicz, M. Galli and T. F. Krauss, *Nat. Nanotechnol.*, 2014, **9**, 19–32.
- 4 A. I. Hochbaum, R. Chen, R. D. Delgado, W. Liang, E. C. Garnett, M. Najarian, A. Majumdar and P. Yang, *Nature*, 2008, **451**, 163–167.
- 5 R. Chen, J. Lee, W. Lee and D. Li, *Chem. Rev.*, 2019, published online, <http://dx.doi.org/10.1021/acs.chemrev.8b00627>.
- 6 A. I. Boukai, Y. Bunimovich, J. Tahir-Kheli, J.-K. Yu, W. A. Goddard III and J. R. Heath, *Nature*, 2008, **451**, 168–171.
- 7 Y. Zhou and M. Hu, *Nano Lett.*, 2016, **16**, 6178–6187.
- 8 W. Liu and M. Asheghi, *J. Appl. Phys.*, 2005, **98**, 123523.
- 9 Y. S. Ju and K. E. Goodson, *Appl. Phys. Lett.*, 1999, **74**, 3005.
- 10 D. Li, Y. Wu, P. Kim, L. Shi, P. Yang and A. Majumdar, *Appl. Phys. Lett.*, 2003, **83**, 2934.
- 11 L. Yang, Y. Yang, Q. Zhang, Y. Zhang, Y. Jiang, Z. Guan, M. Gerboth, J. Yang, Y. Chen, D. Greg Walker, T. T. Xu and D. Li, *Nanoscale*, 2016, **8**, 17895–17901.
- 12 J. Lim, K. Hippalgaonkar, S. C. Andrews and A. Majumdar, *Nano Lett.*, 2012, **12**, 2475–2482.
- 13 J.-K. Yu, S. Mitrovic, D. Tham, J. Varghese and J. R. Heath, *Nat. Nanotechnol.*, 2010, **5**, 718–721.
- 14 P. E. Hopkins, C. M. Reinke, M. F. Su, R. H. Olsson, E. a. Shaner, Z. C. Leseman, J. R. Serrano, L. M. Phinney and I. El-Kady, *Nano Lett.*, 2011, **11**, 107–112.

- 15 S. Alaie, D. F. Goettler, M. Su, Z. C. Leseman, C. M. Reinke and I. El-Kady, *Nat. Commun.*, 2015, **6**, 7228.
- 16 E. Dechaumphai and R. Chen, *J. Appl. Phys.*, 2012, **111**, 073508.
- 17 A. Jain, Y. J. Yu and A. J. H. McGaughey, *Phys. Rev. B - Condens. Matter Mater. Phys.*, 2013, **87**, 195301.
- 18 N. K. Ravichandran and A. J. Minnich, *Phys. Rev. B*, 2014, **89**, 205432.
- 19 J. Lee, W. Lee, G. Wehmeyer, S. Dhuey, D. L. Olynick, S. Cabrini, C. Dames, J. J. Urban and P. Yang, *Nat. Commun.*, 2017, **8**, 14054.
- 20 J. Tang, H. T. Wang, D. H. Lee, M. Fardy, Z. Huo, T. P. Russell and P. Yang, *Nano Lett.*, 2010, **10**, 4279–4283.
- 21 J. Lim, H.-T. Wang, J. Tang, S. C. Andrews, H. So, J. Lee, D. H. Lee, T. P. Russell and P. Yang, *ACS Nano*, 2016, **10**, 124–132.
- 22 Y. Sharvin, *Sov. Phys. JETP*, 1965, **21**, 655.
- 23 R. Prasher, *Nano Lett.*, 2005, **5**, 2155–2159.
- 24 D. Li and A. J. H. McGaughey, *Nanoscale Microscale Thermophys. Eng.*, 2015, **19**, 166–182.
- 25 J. Maire and M. Nomura, *Jpn. J. Appl. Phys.*, 2014, **53**, 06JE09.
- 26 M. Nomura and J. Maire, *J. Electron. Mater.*, 2015, **44**, 1426–1431.
- 27 J. Maire, R. Anufriev, T. Hori, J. Shiomi, S. Volz and M. Nomura, *Sci. Rep.*, 2018, **8**, 4452.
- 28 L. Yang, Q. Zhang, Z. Cui, M. Gerboth, Y. Zhao, T. T. Xu, D. G. Walker and D. Li, *Nano Lett.*, 2017, **17**, 7218–7225.
- 29 T. H. P. Chang, *J. Vac. Sci. Technol.*, 1975, **12**, 1271–1275.
- 30 M. a. Meitl, Z.-T. Zhu, V. Kumar, K. J. Lee, X. Feng, Y. Y. Huang, I. Adesida, R. G. Nuzzo and J. a. Rogers, *Nat. Mater.*, 2006, **5**, 33–38.
- 31 M. C. Wingert, Z. C. Y. Chen, S. Kwon, J. Xiang and R. Chen, *Rev. Sci. Instrum.*, 2012, **83**, 114901.
- 32 A. L. Moore and L. Shi, *Meas. Sci. Technol.*, 2010, **22**, 015103.
- 33 Q. Zhang, Z. Cui, Z. Wei, S. Y. Chang, L. Yang, Y. Zhao, Y. Yang, Z. Guan, Y. Jiang, J. Fowlkes, J. Yang, D. Xu, Y. Chen, T. T. Xu and D. Li, *Nano Lett.*, 2017, **17**, 3550–3555.
- 34 L. Yang, Y. Tao, J. Liu, C. Liu, Q. Zhang, M. Akter, Y. Zhao, T. T. Xu, Y. Xu, Z. Mao, Y. Chen and D. Li, *Nano Lett.*, 2019, **19**, 415–421.
- 35 J. Yang, Y. Yang, S. W. Waltermire, X. Wu, H. Zhang, T. Gutu, Y. Jiang, Y. Chen, A. a. Zinn, R. Prasher, T. T. Xu and D. Li, *Nat. Nanotechnol.*, 2011, **7**, 91–95.
- 36 K. Termentzidis, T. Barreateau, Y. Ni, S. Merabia, X. Zianni, Y. Chalopin, P. Chantrenne and S. Volz, *Phys. Rev. B*, 2013, **87**, 125410.
- 37 W. Park, J. Sohn, G. Romano, T. Kodama, A. Sood, J. S. Katz, B. S. Y. Kim, H. So, E. C.

- Ahn, M. Asheghi, A. M. Kolpak and K. E. Goodson, *Nanoscale*, 2018, **10**, 11117–11122.
- 38 M. Nomura, private communication, August, 2015.
- 39 R. M. Costescu, M. A. Wall and D. G. Cahill, *Phys. Rev. B*, 2003, **67**, 054302.
- 40 E. Dechaumphai, D. Lu, J. J. Kan, J. Moon, E. E. Fullerton, Z. Liu and R. Chen, *Nano Lett.*, 2014, **14**, 2448–2455.
- 41 Y. K. Koh, Y. Cao, D. G. Cahill and D. Jena, *Adv. Funct. Mater.*, 2009, **19**, 610–615.
- 42 B. Nikolić and P. B. Allen, *Phys. Rev. B*, 1999, **60**, 3963–3969.
- 43 R. Prasher, *Phys. Rev. B - Condens. Matter Mater. Phys.*, 2006, **74**, 165413.
- 44 R. S. Prasher and P. E. Phelan, *J. Appl. Phys.*, 2006, **100**, 063538.
- 45 D. L. Nika, a. I. Cocemasov, C. I. Isacova, a. a. Balandin, V. M. Fomin and O. G. Schmidt, *Phys. Rev. B - Condens. Matter Mater. Phys.*, 2012, **85**, 205439.
- 46 X. Zianni, V. Jean, K. Termentzidis and D. Lacroix, *Nanotechnology*, 2014, **25**, 465402.
- 47 F. H. Stillinger and T. A. Weber, *Phys. Rev. B*, 1985, **31**, 5262–5271.
- 48 T. Schneider and E. Stoll, *Phys. Rev. B*, 1978, **17**, 1302–1322.
- 49 D. Şopu, J. Kotakoski and K. Albe, *Phys. Rev. B - Condens. Matter Mater. Phys.*, 2011, **83**, 245416.

TOC:



Phonon mean free path increases with fin width, boosting the Sharvin resistance at the constrictions.